Robust and Manufacturable Lithium Lanthanum Titanate-Based Solid-State Electrolyte Thin Films Deposited in Open Air

Mohammed Sahal, Jie Molloy, Venkateshwaran Ravi Narayanan, Leila Ladani, Xiaochuan Lu, and Nicholas Rolston*

Read Online

ACCESS | Metrics & More | Article Recommendations | Supporting Information

ABSTRACT: State-of-the-art solid-state electrolytes (SSEs) are limited in their energy density and processability based on thick, brittle pellets, which are generally hot pressed in vacuum over the course of several hours. We report on a high-throughput, open-air process for printable thin-film ceramic SSEs in a remarkable one-minute time frame using a lithium lanthanum titanium oxide (LLTO)-based SSE that we refer to as robust LLTO (R-LLTO). Powder XRD analysis revealed that the main phase of R-LLTO is polycrystalline LLTO, accompanied by selectively retained crystalline precursor phases. R-LLTO is highly dense and closely matched to the stoichiometry of LLTO with some heterogeneity throughout the film. A minimal presence of lithium carbonate is identified despite processing fully in ambient conditions. The LLTO films exhibit remarkable mechanical properties, demonstrating both flexibility with a low modulus of ∼35 GPa and a high fracture toughness of >2.0 MPa$\sqrt{m}$. We attribute this mechanical robustness to several factors, including grain boundary strengthening, the presence of precursor crystalline phases, and a decrease in crystallinity or ordering caused by ultrafast processing. The creation of R-LLTO—a ceramic material with elastic properties that are closer to polymers with higher fracture toughness—enables new possibilities for the design of robust solid-state batteries.
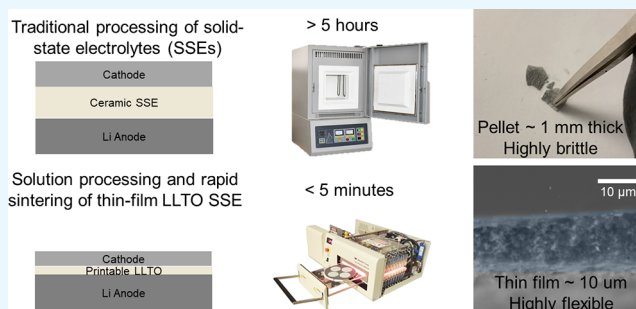
1. INTRODUCTION

Lithium-ion batteries are favored as a power source for consumer electronics, electric cars, and electric grids due to their high energy and power density as well as their low greenhouse gas emissions.[1−3] Traditional Li-ion batteries use organic solvent-based liquid electrolytes that are highly volatile, flammable, and nonergonomic, raising safety and design concerns.[4] All solid-state lithium batteries, on the other hand, improve battery safety by eliminating major concerns associated with liquid electrolytes, such as high temperature swelling and leakage under external forces. Furthermore, solid-state electrolytes (SSEs) increase capacity by introducing additional active material space created by eliminating the space occupied by the inherent safety components—namely, the separator—required for liquid electrolyte batteries.[5] Nevertheless, to fully realize their potential to replace liquid electrolytes, SSEs must overcome significant challenges such as low ionic conductivity, poor mechanical properties, and limited scalability.[6−12] An ideal SSE for all Li-SSBs should have a high ionic conductivity, reaching values in the 10^{-2} S cm^{-1} range, as obtained for commonly used liquid electrolytes (LiPF$_6$ in an ethylene carbonate/diethylene carbonate solvent).[13] However, dense, ∼100 μm-thick, thin-film SSEs with ionic conductivities of 10^{-4} to 10^{-3} S cm^{-1} have been previously demonstrated as feasible for battery applications.[14,15] In addition to ionic conductivity, the

SSE material is expected to be chemically stable when in contact with Li-ion battery cathodes and anodes.[16−18] Cost-effective synthesis and a scalable thin-film fabrication process that does not compromise robustness are also highly desired.[9]

Aside from ionic conductivity, chemical stability, and cost-effective manufacturing, an SSE also requires suitable mechanical properties for a range of applications.[19] These mechanical properties include the elastic, plastic, and fracture properties of the SSE.[20] Mechanical properties are a determining factor for the following factors affecting SSE performance: (1) Lithium dendrite suppression: High elastic stiffness (<10 GPa[19,21]) and shear modulus of the SSE should be equal[22] to or greater than those of Li, which have been experimentally determined as 1.9[23] and 3.1[24] GPa. (2) High fracture toughness: High fracture toughness allows for a thinner electrolyte, enabling desirable cell operational properties like high power output during discharge, high energy density, and lower cell resistance.[25,26] Recent studies[25,27] discovered that the critical current, which causes cell

failure when dendrites grow during charging, is linked to the solid electrolyte's fracture strength and grain boundary conductivity. As the fracture strength increases, the critical current also increases. (3) Low hardness and elastic modulus: Elastic, soft, and ductile SSEs can more effectively accommodate the stresses and strains that are induced at the electrode−SSE interface during lithium intercalation and deintercalation.[26]

EV manufacturers have set a target for solid-state batteries (SSBs) to attain energy densities of approximately 900−1000 Wh/L (around 400 Wh/kg) before considering a shift from existing lithium-ion cells to SSBs.[28] However, achieving such high energy densities using current battery architectures would necessitate SSEs with high fracture toughness that enable thin-film thicknesses of 50 μm or less. Among SSEs, inorganic SSEs exhibit higher bulk ionic conductivity compared to polymer SSEs. Conversely, polymers have superior ductility and deformability based on their elastic properties (low modulus and hardness) along with plasticity when compared to inorganic SSEs.[29−31] Improving the ductility and deformability of inorganic SSEs could enhance their potential for use as SSEs in practical applications and facilitate a seamless transition from current lithium-ion cells to solid-state batteries (SSBs).

In this work, we demonstrate an ultrahigh-throughput, fully open-air processing route with significantly improved mechanical properties for an SSE with a polycrystalline lithium lanthanum titanate, $Li_{0.3}La_{0.56}TiO_3$ (LLTO), phase. LLTO is a perovskite-based (ABO_3) SSE, which has Li and La as the A-site cations contained within TiO_6 octahedra. LLTO has been studied in both polycrystalline pellet and thin-film forms.[32] Pellets are typically prepared by either solid-state or sol−gel processing routes. Thin films can be produced from a variety of methods, including physical vapor deposition, chemical vapor deposition, sputtering, evaporation, and solution-processing.[33−35] Previously, composite pellets made up of LLTO with both porous and nonporous components demonstrated outstanding fracture toughness properties, measuring at approximately 2 MPa*$m^{0.5}$. Nevertheless, there is currently no literature available that confirms a comparable fracture toughness value for an LLTO thin film, which is essential for achieving high energy density.

Another challenge faced by LLTO SSEs is their low overall ionic conductivity, which results from the combined effect of two distinct conduction mechanisms. First, as the concentration of Li increases within the structure, there is a reduction in bulk conductivity due to localized distortions of the lattice, which causes an increase in the migration energy barrier and slows down ion conduction. Second, low grain boundary conductivity poses a challenge in these polycrystalline materials, and the existence of boundaries frequently results in a total ionic conductivity of approximately 10^{-5} S/cm.[6,33,34,36−39] The grain boundary resistance relates to potential secondary phases (such as undesirable Li_2CO_3) or structural deformations that can deplete both Li and La at grain boundaries.

High-temperature sintering and time required to densify most tape-cast ceramic SSEs also contribute to the manufacturing costs.[40] Previous work has also shown that it is difficult to produce thin films with ionic conductivity comparable to those in mm-thick sintered pellets using thin-film deposition methods.[33] Most of the previously demonstrated work has used methods that also may not be readily translatable or sufficiently low-cost for manufacturing.[41] This work not only showcases the improved mechanical properties of LLTO but also introduces a scalable, open-air processing technique that is

suitable for in-line manufacturing, enabling the production of dense and mechanically robust thin-film LLTO SSEs.

2. RESULTS

2.1. X-ray Diffraction (XRD). The XRD spectra for the R-LLTO film, an unprocessed precursor mixture of Li_2CO_3, TiO_2, and La_2O_3, and a reference pattern for polycrystalline $Li_{0.3}La_{0.56}TiO_3$:[42] ICDD 04-014-0049) are shown in Figure 1. Clearly, the peaks of the R-LLTO XRD spectrum differ
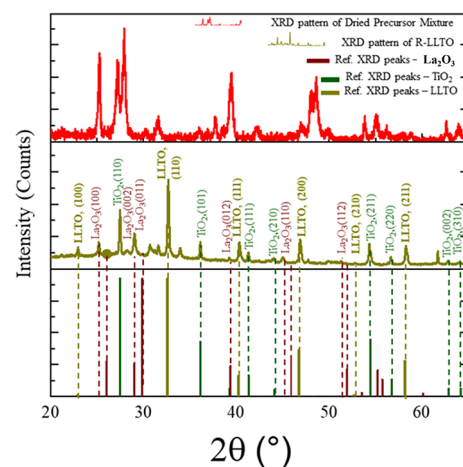

Figure 1. X-ray diffraction scans of the precursor mixture, R-LLTO SSE, and reference powder XRD spectra for LLTO ($Li_{0.3}La_{0.56}TiO_3$− ICDD 04-014-0049), TiO_2 (ICDD 04-002-8295), and La_2O_3 (ICDD 04-006-5083).

significantly from those of the unprocessed precursor mixture of Li_2CO_3, TiO_2, and La_2O_3 shown in Figure 1. Peaks in the R-LLTO XRD spectrum are associated with both the newly formed LLTO phase and the retained precursors TiO_2 and La_2O_3. The LLTO-phase peaks in the R-LLTO XRD spectrum are indexed and show a clear correspondence with the 2-theta peak positions and relative intensity variation seen in polycrystalline $Li_{0.3}La_{0.56}TiO_3$ (PDF47: ICDD 04-014-0049). Figure 1 also shows indexed peaks for the retained precursor phases, TiO_2 (ICDD[42] 04-002-8295) and La_2O_3 (ICDD[42] 04-006-5083). Peaks for TiO_2 show clear correspondence with the reference peaks, while peaks for La_2O_3 show a shift in the peak position. However, the R-LLTO XRD spectrum shows hardly any correspondence with the diffraction peaks of the precursor Li_2CO_3 phase, indicating that lithium is fully consumed during the processing steps to form the LLTO phase. Semiquantitative phase estimation using HighScore software revealed that the R-LLTO film contains an approximately 48% polycrystalline LLTO phase, while the proportions of retained precursor TiO_2 and La_2O_3 phases are 40 and 12%, respectively.

2.2. Scanning Electron Microscopy (SEM). To better understand the microstructure and composition of R-LLTO, secondary electron (SE) and backscattered electron (BSE) imaging was performed. The R-LLTO film density across its thickness and at the R-LLTO-Si substrate interface was analyzed. Figure 2a,b shows two distinct regions in both BSE and SE images, one darker and one brighter. The dark region in the SE image, however, is brighter in the BSE image. These correspond to two distinct phases within the film. EDS analysis of the spots shown in Figure 3a,b revealed that the darker region in the SE image corresponds to a La-rich phase, whereas the darker region in the BSE image corresponds to a Ti-rich phase.
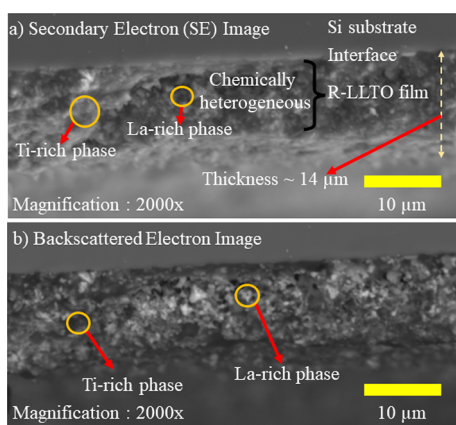
Figure 2. (a) Cross-sectional scanning electron microscope (SE) image of an R-LLTO film revealing chemical heterogeneity, with distinct La-rich and Ti-rich phases complementing each other. (b) In a corresponding backscattered electron (BSE) image of the same R-LLTO film cross section, the contrast for the La-rich and Ti-rich phases is reversed compared to the SE image.
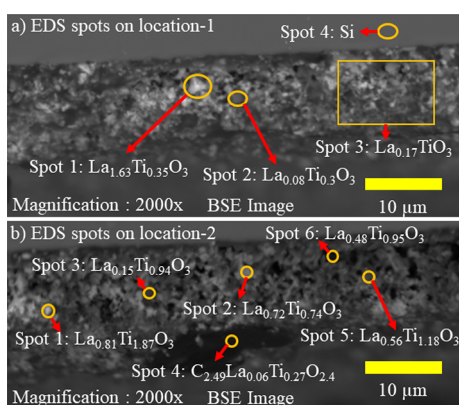
Figure 3. (a) Molar compositions of EDS spots at location-1 on the cross section of an R-LLTO film. (b) Molar compositions of EDS spots at location-2 on the cross section of an R-LLTO film. Spots 5 and 6, which indicate a composition close to the $Li_{0.3}La_{0.56}TiO_3$ phase, are visible as medium-gray contrast in the backscattered electron (BSE) image.

Alternatively, the brighter region in the BSE image revealed a phase rich in La, whereas the brighter region in the SE image revealed a phase rich in Ti. Thus, the presence of densely packed complementary phases eliminates the possibility of dark regions in both the SE and BSE images being caused by gaps or low thin-film density. As shown in Figure 2a, the region of the R-LLTO film that extends through its thickness to the interface with the Si substrate is characterized by chemical heterogeneity, as it exhibits a more or less uniform mixture of these complementary phases.

2.3. Energy-Dispersive Spectroscopy (EDS). EDS analysis is semiquantitative, and it does not detect Li in the phase composition due to a lack of instrument sensitivity at such low atomic numbers. The EDS spectra of spots on BSE images shown in Figure 3a,b are shown in Figures S1 and S2. EDS analysis was performed on four spots of location-1 in the R-LLTO film, which is highlighted on the BSE image, as shown in Figure 3a.

The quantification and comparison of the Ti L_α and K_α and La L_α peaks shown in Figures S1 and S2 revealed the dominant element present in each location. Ti L_α and K_α peaks have

energies of 0.452 and 4.508 eV, respectively, while the La L_α peak has an energy of 4.65 eV. The La L_α peak at 4.65 eV has a much higher intensity than the Ti K_α peak at 4.508 eV for spot 1 of the BSE image shown in Figure 3a. This corresponds to the brighter visual appearance seen in spot 1 of Figure 3a, which is expected for a heavier La-rich phase.

Similarly, spots 2 and 3 on the BSE image shown in Figure 3a appear darker and have Ti K_α peaks with higher intensities than La L_α peaks. Spot 4 of the BSE image shown in Figure 3a is obtained on a substrate, with only the Si K_α peak at 1.739 eV. Additionally, Figure 3a shows the molar compositions determined for spots 1−4 of location-1 in the R-LLTO film. The molar composition of the La-rich phase visible as white in the BSE image shown in spot 1 in Figure 3a is $La_{1.6}Ti_{0.34}O_3$, which may indicate that the La_2O_3 precursor lacks sufficient Li_2O and TiO_2 precursors locally to form the LLTO phase in the white regions of the BSE image. The average molar composition of all spots in Figure 3a is $La_{0.63}Ti_{0.55}O_3$, indicating that the surveyed area is Ti-deficient. EDS analysis was conducted on six additional spots on location-2 of the R-LLTO film, as described in Figure 3b. In Figure 3b, spots 1 and 2 showed slightly higher La L_α peak intensity than Ti L_α peak intensity, whereas spots 3 and 4 displayed higher Ti L_α peak intensity compared to La L_α peak intensity.

Spot 4 in Figure 3b shows the presence of a carbon impurity and is very dark, as expected for a much lighter carbon-rich phase in a BSE image. Spots 5 and 6 in Figure 3b, which appear medium gray in the BSE image, have the closest molar compositions to the $Li_{0.3}La_{0.56}TiO_3$ phase with $La_{0.56}Ti_{1.18}O_3$ and $La_{0.48}Ti_{0.95}O_3$, respectively. This suggests that the LLTO crystalline phase may be visible as medium gray in the BSE image. The average molar composition of all spots in Figure 3b is $La_{0.55}Ti_{1.1}O_3$, indicating that the surveyed area is close stoichiometrically to the precursor molar composition of $Li_{0.3}La_{0.56}TiO_3$. Further, the automatic estimates for element mass percentages provided by the built-in EDS software may be less precise on an individual spot as the La L_α and Ti K_α peaks overlap due to their proximity on the energy spectrum. Table S1 outlines the method for calculating the molar compositions of individual spots and the average molar compositions for location-1 and location-2 in the R-LLTO film, which are shown in Figure 3a,b. Table S2 shows the average molar composition of La, Ti, and O based on their visual appearance in the BSE image shown in Figure 2.

2.4. X-ray Photoelectron Spectroscopy (XPS) Analysis. The surface chemistry of the LLTO thin-film surface was investigated using XPS analysis to probe for any detrimental surface carbonate layers and to quantify the presence of Li. Figure S3 shows the spots on the LLTO film surface where the XPS spectrum was collected. The presence of Li was confirmed at all the locations, as shown in the respective Li elemental spectra in Figure S4. Table S3 summarizes the molar ratios of Li:La:Ti:O for the XPS spots shown in Figure S3. The average Li:O stoichiometry for the four sites was 0.36:3.58 or 0.3:3, which is close to Li:O in the $Li_{0.3}La_{0.56}TiO_3$ phase. However, the average La:O and Ti:O stoichiometries for the four spots were 0.1:3 and 0.4:3, which were lower than the corresponding stoichiometries of 0.56:3 and 1:3 in the $Li_{0.3}La_{0.56}TiO_3$ phase. Note that XPS only probes a few atomic layers, and the average La:Ti:O ratios determined by the more bulk-like EDS technique revealed that the average La:Ti:O stoichiometry sampled for 9 different spots is ~0.59:0.92:3, which is closer to that in the $Li_{0.3}La_{0.56}TiO_3$ phase. The XPS analysis of Li:O and EDS
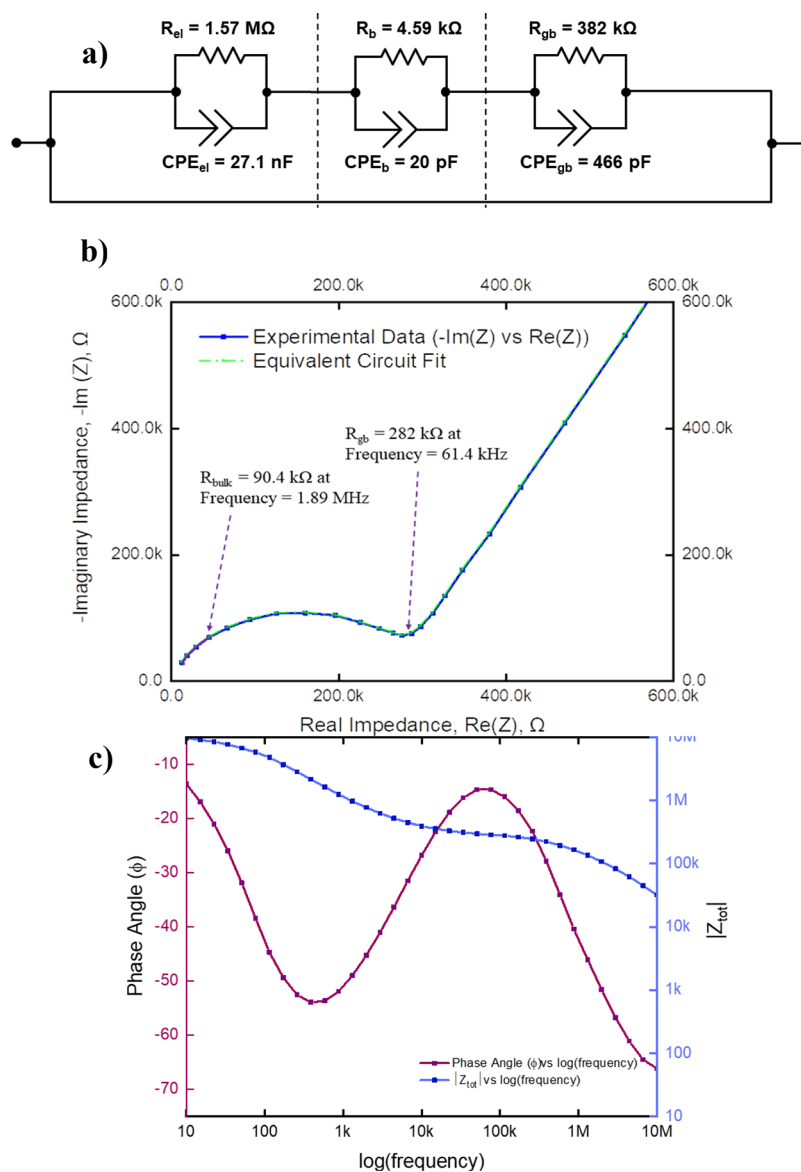
Figure 4. (a) Values provided were used to model an equivalent circuit impedance fit for the Nyquist plot displayed below. (b) Experimentally obtained Nyquist plot for the LLTO film with impedance response generated by the equivalent circuit. (c) Complementary Bode plot showing the phase angle (Φ) and magnitude of the overall impedance ($|Z_{tot}|$) vs log(frequency).

analysis of La:Ti:O suggest that the overall composition of the R-LLTO film is very similar to Li:La:Ti:O in the $Li_{0.3}La_{0.56}TiO_3$ phase, with slight variations caused by the precursor phases.

There is evidence for a small amount of lithium carbonate on the surface of R-LLTO. As shown in Figure S5, the C 1s peak at 288.6 eV indicates an O−C=O bond, and the overall Li 1s:C 1s ratio is 1.95:3, which is comparable to the 2.3:3 expected Li 1s:C 1s molar ratio for an equal mixture of Li_2CO_3 and $Li_{0.3}La_{0.56}TiO_3$. It is important to note that the XPS experiment was performed without any surface cleaning or etching before measurement. All the processing for R-LLTO was also done in an open-air environment. Since XPS can detect La and Ti on the unetched surface, it suggests that the thickness of lithium carbonate present is likely in the nanometer range.

2.5. Electrochemical Impedance Spectroscopy (EIS). Figure S6 showing an in-plane ion blocking electrode configuration on R-LLTO was used for EIS measurements. Silver electrodes are prepared using a rapid drying silver ink. Figure 4b,c shows a Nyquist plot and a complementary Bode

plot constructed from impedance data acquired in the frequency range of 10 Hz to 10 MHz for the R-LLTO. The complementary Bode plot shows two plateaus, which correspond to the bulk and grain boundary semicircles seen in the Nyquist plot. An equivalent circuit also shown in Figure 4a was used to fit impedance semicircles in low, medium, and high frequency ranges to extract the bulk and grain boundary impedances and to estimate electrode contact resistance.[13,43−45] Li+ transport and conduction through grain boundaries and thin-film bulk are characterized by the ionic conductivities calculated according to eqs 1−4.[46]

$$\text{film ionic conductivity}\left(\frac{S}{cm}\right), \sigma_{ion-film}$$

$$= \frac{l\ (cm)}{R_{total}\ (\Omega) \times A\ (cm^2)} \tag{1}$$
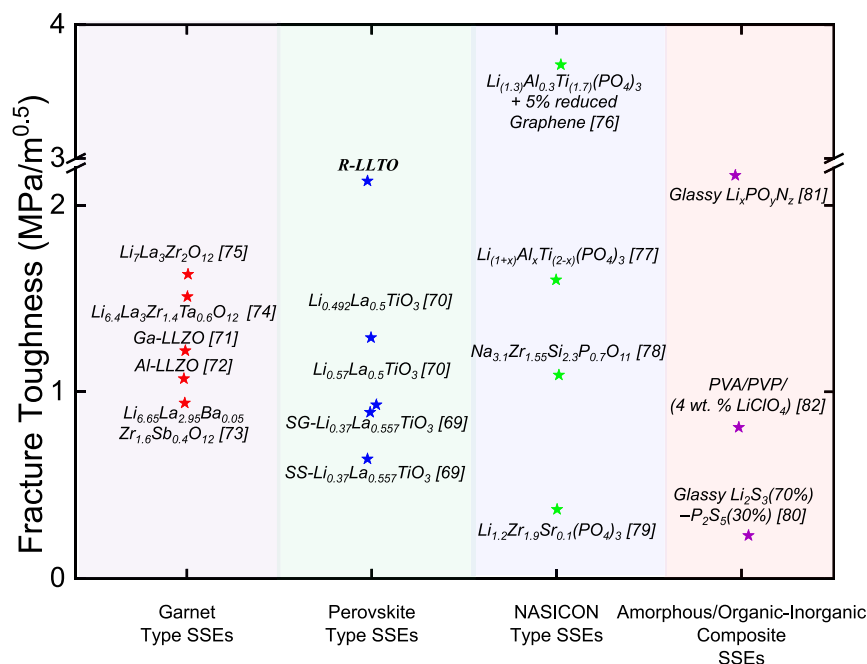
Figure 5. Comparison of R-LLTO's high fracture toughness with recently reported garnet SSEs, other perovskite SSEs, NASICON-type SSEs, and amorphous/composite SSEs.

bulk ionic conductivity $\left(\dfrac{S}{cm}\right)$, $\sigma_{ion-bulk}$

$$= \frac{l\ (cm)}{R_{bulk}\ (\Omega) \times A\ (cm^2)} \qquad (2)$$

grain boundary ionic conductivity $\left(\dfrac{S}{cm}\right)$, σ_{ion-gb}

$$= \frac{l\ (cm)}{R_{gb}\ (\Omega) \times A\ (cm^2)} \qquad (3)$$

$$R_{total}\ (\Omega) = R_{bulk}\ (\Omega) + R_{GB}\ (\Omega) \qquad (4)$$

σ_{total}, σ_{bulk}, and σ_{gb} for the thin film were 2.17×10^{-5}, 7.2×10^{-5}, and 3.11×10^{-5} S/cm, respectively. The ionic conductivity calculations are shown below Figure S6 in the supplemental document. As shown in Figure 4, these conductivity values correspond to the expected high frequency ranges > MHz for bulk and mid frequency ranges (kHz > MHz) for grain boundary ionic conduction. Individual ionic conductivity values for the inorganic electrolyte[29,47−52] such as LGPS, LTP, and LGP with LISICON- and NASICON-type frameworks are higher than that of the R-LLTO film. The blocking effect[53,54] of LLTO grain boundaries reduces its overall ionic conductivity.

According to the literature, the main causes of ionic conduction blocking at grain boundaries are (1) space charge effects and (2) microphase segregation that reduces the carrier concentration.[55,56] The presence of local undesirable Ti-rich microphase segregation in R-LLTO grain boundaries may be the primary cause of the ionic conduction blocking mechanism. This is supported by the local stoichiometric deviation of individual EDS analysis spots from the bulk composition ($Li_{0.3}La_{0.56}TiO_3$), which is discussed in detail in Section 2.3. The low grain boundary ionic conductivity can be improved using a variety of approaches, such as modifying the sintering temperature[57] and atmosphere,[58] Sr^{2+} doping at La^{3+} lattice sites,[59] and increasing phase density.[60]

2.6. Mechanical Properties. *2.6.1. Hardness and Elastic Modulus.* Nanoindentation was used to estimate the hardness and elastic modulus of both sintered and unsintered R-LLTO films. The average hardness of the unsintered R-LLTO film is 0.68 ± 0.04 GPa, and its average elastic modulus is 15.58 ± 7.23 GPa. In contrast, the sintered R-LLTO film has a significantly higher average elastic modulus of 35.3 ± 14.64 GPa and a higher average hardness of 1.95 ± 1.04 GPa. Figure S7 shows the load−displacement graphs on the sample for two representative indents for both experiments. Clearly, the maximum load increases significantly with the increase of the depth to 5000 nm. The large standard deviation in the elastic modulus can be attributed to the presence of the indentation size effect (ISE)[61] and the fact that the surface is rougher than 1 μm, as shown in Figure S8.

2.6.2. Fracture Toughness. The Vickers microhardness test indenter was used to induce a crack on the LLTO film surface at a force of about 9.8 N. The crack size and indenter load applied by the Vickers hardness tester, as well as the nanohardness and Young's modulus values obtained through nanoindentation measurements, were used to determine fracture toughness[62] of the LLTO film in units of $\frac{N}{m^{1.5}}$, as shown in eq 5[62]

$$\text{fracture toughness, } K_{Ic} = 0.016\left(\frac{E}{H}\right)^{0.5}\left(\frac{P}{C^{1.5}}\right) \qquad (5)$$

The average modulus to nanohardness ratio for the LLTO film was 19.34, and the size of the crack made by the Vickers indenter at a 9.8 N load was 47.1 μm. The fracture toughness of the LLTO film was determined to be 2.13 ± 0.06 MPa$\sqrt{m}$.

Figure 5 compares the fracture toughness value of the R-LLTO film to that of other perovskites,[63,64] garnet,[65−69] NASICON-type,[70−73] and amorphous[74,75] or organic−inorganic composite[76] SSEs reported in the literature. As shown in Figure 5, the R-LLTO SSE film has a higher fracture toughness than LLTO SSEs with different Li molar compositions (0.37, 0.49, and 0.56) and LLTO SSEs synthesized using sol−gel and

solid-state reaction methods that differ from the solution processing method used for the R-LLTO SSE. For the LLTO SSEs shown in Figure 5, the H/E ratio, which represents the elastic strain at failure,[77] is the greatest for R-LLTO at approximately 0.05 and the lowest for $Li_{0.49}La_{0.5}TiO_3$ at around 0.03. In comparison to non-LLTO SSEs such as the NASICON-type Li and Na SSEs, $Li_{1+x}Al_xTi_{2-x}(PO_4)_3$ (LATP), and Von Alpen (VA)-type NASICON $(Na_{3.1}Zr_{1.55}Si_{2.55}P_{0.7}O_{11})$, R-LLTO exhibits higher fracture toughness values, as shown in Figure 5. The higher fracture toughness of R-LLTO compared to other NASICON and garnet SSEs can be explained by its ability to undergo plastic deformation, as suggested by its relatively lower hardness value in Figure 6. However, the fracture
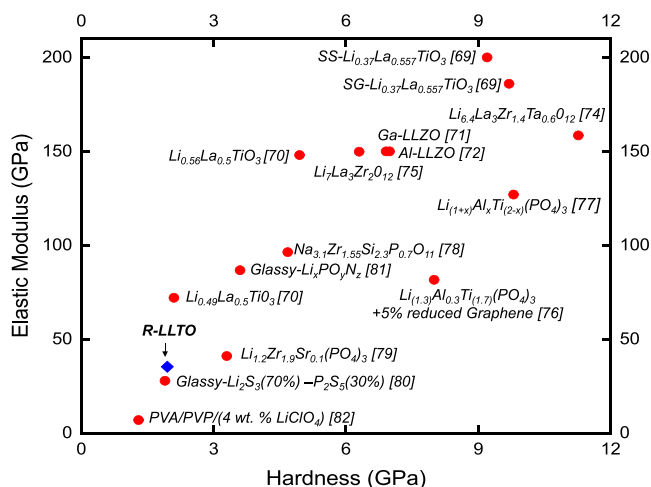
Figure 6. R-LLTO has a slightly higher hardness and modulus than amorphous/polymer composite SSEs, but it has much lower values than recently reported garnet SSEs, other perovskite SSEs, NASICON-type SSEs, and amorphous/composite SSEs, as desired for a robust SSE.

toughness of $Li_{1+x}Al_xTi_{2-x}(PO_4)_3$ (LATP) with 5% reduced graphene is higher than that of the R-LLTO. The presence of graphene oxide in the LATP matrix may act as crack arresting locations, improving the fracture toughness of the LATP. Table S5 presents the elastic modulus, hardness, and fracture toughness of solid-state electrolytes (SSEs) belonging to perovskite, garnet, and NASICON-type SSEs, which were discussed in the preceding and current sections.

3. DISCUSSION

Several factors affect the performance of an SSE film or pellet. This section will focus on three key aspects that are crucial for achieving optimal overall performance: chemomechanical integrity, manufacturability, and scalability.

3.1. Plastic Deformation and Fracture Energy. If all other factors are kept constant in eq 5, the variation in the E/H ratio from 17 to 34 results in an overall fracture toughness change by a factor of merely 0.09 MPa$\sqrt{\text{m}}$. Therefore, it is not the E/H ratio but rather the plasticity of the material that has the largest effect on increasing the fracture toughness. This is further supported by the ability of R-LLTO to plastically deform, as shown by the low hardness value for R-LLTO in Figure 6. K_{IC} depends on the energy required to break apart the bonds of a material and of plastic deformation in the material as shown in eq 9. The bonding is identical to LLTO, and therefore, we deduce that the higher fracture energy for R-LLTO is due to plastic deformation. $K_{IC\text{-bond}}$ is limited by the bonding of the

material, and it is not expected that a significant change in the bonding configuration will occur in R-LLTO.

$$K_{IC} = K_{IC-bond} + K_{IC-plastic\ deformation} \tag{6}$$

This fracture toughness is more than an order of magnitude greater than typical polycrystalline ceramic[78] coatings. We hypothesize that the mechanism for the improvement in fracture toughness is due to increased plastic deformation from the comparably low hardness.

3.2. Low Elastic Modulus and Hardness for R-LLTO. The modulus and hardness values of the R-LLTO are much lower when compared to other inorganic SSEs, as shown in Figure 6. This is a highly surprising result and could be due to a few different factors:

(1) Microstructure: The R-LLTO film's unique microstructure is hypothesized to be the most crucial factor in achieving low modulus and hardness values. The elastic modulus of R-LLTO can be reduced through deformation accommodation due to the combined effects of small crystallite sizes in its microstructure and grain boundaries inducing dislocations, an effect also observed in metals.

(2) Reduced crystallinity: The lower modulus and hardness of R-LLTO could be attributed to the effect of reduced crystallinity based on the presence of precursor phases (Figure 1), which as noted above have an extremely low modulus and hardness.

(3) Processing method: The processing method of R-LLTO also potentially contributes to the different mechanical properties since the thin film is produced directly from the solution phase and no pressure is applied, which would maximize density and lead to increased stiffness with reduced void space. There is the possibility of nanostructuring in the R-LLTO, which could partially account for these properties.

The low hardness and modulus for R-LLTO are advantageous for processability. Additionally, the modulus is sufficiently high so that the shear modulus of the LLTO film, as determined by eq 6, is ~2 times greater than that of Li metal, which is necessary to suppress Li dendrite nucleation.[79] In the equations below, B is the bulk modulus and G is the shear modulus that can be calculated from the Young's modulus and Poisson ratio (ν, assumed to be 0.26 for LLTO[80]):

$$G = \left(\frac{E}{2(1+\nu)}\right) \tag{7}$$

$$B = \left(\frac{E}{3(1-2\nu)}\right) \tag{8}$$

$$\text{Pugh factor} = \left(\frac{B}{G}\right) \tag{9}$$

The Pugh factor calculated using eqs 6, 7, and 8 for the R-LLTO film is 1.76, a value that indicates that the R-LLTO is categorized as a ductile material.[26] The ductility of the LLTO film improves fracture toughness and allows for better stress−strain accommodations, which is critical for resisting Li dendrite penetration. During Li cycling, the ductile SSE can slow the growth of interface cracks. In addition, the R-LLTO should have a sufficiently high shear modulus to suppress. Thus, the R-LLTO investigated in this study holds promise as a mechanically robust SSE for lithium batteries.

3.3. Manufacturability. Table S4 and Figure S9 shows a comparison of the processing time (h) and ion conduction (S/(cm m)) values of R-LLTO with SSE pellets,[81−83] inorganic thin films,[29,47−52] and organic−inorganic composites.[84−88] This comparison provides insight into the relationship between throughput and critical electrolyte performance. The time spent converting precursors to the final form of the SSE, either a pellet or a thin film, is referred to as processing time. Ionic conductivity per thickness of the SSE provides information about the thickness required to achieve the most desirable Li⁺ ion transport rate that may be possible for the electrolyte. Higher ionic conductivity per thickness values and shorter processing durations are directly related to enhanced SSE performance and lithium battery manufacturability.

Figure S9 shows that the R-LLTO film is within an order of magnitude of the ionic conductivity per thickness value for recently reported SSE pellets,[81−83] thin films,[47,52,84−88] and organic−inorganic composites while reducing processing time by more than five times on average. Unlike LLTO, LISICON- and NASICON-type SSEs require much thicker films to achieve the high ionic conductivity shown in Figure S9. They also have poor mechanical properties, as illustrated by their fracture toughness values in Figure 5. When compared to LISICON- and NASICON-type SSEs, LiPON and garnet-type SSEs, such as LLZO, may provide structural strength at a lower thickness. They, however, have higher defect generation energies than in LLTO[89] and are more sensitive to moisture and atmospheric conditions, implying that other materials are more sensitive to processing conditions to achieve the desired level of ionic conductivity and structural stability.

As shown in Figure S9, the R-LLTO SSE film has the shortest processing time of any SSE reported and therefore demonstrates excellent compatibility with large-scale in-line manufacturing. Furthermore, this work can readily be applied to other inorganic SSEs, such as LLZO, which are more electrochemically stable against Li to enable manufacturability.

3.4. Scalability. Open-air stability, mechanical robustness, and a desired ionic conductivity per thickness in the range are essential, while reducing processing times is always desired, even if it is not as important for large-scale manufacturability of SSE films. Furthermore, the thickness of SSEs required for various battery engineering applications may vary. This is much easier to achieve with the blade coating process, as by simply adjusting the blade height, a wide range of thicknesses can be attained without compromising the density of the film; this is much more difficult to achieve with traditional pressing methods to produce pellets. Blade coating can also uniformly coat wafer-scale to small surfaces. As shown in Figure 6, inorganic SSE thin films have lower average ionic conduction values than organic−inorganic composites; the advantage of organic−inorganic composites in ionic conduction over inorganic SSEs comes at the expense of longer processing times. However, in terms of scalability, inorganic SSE thin films with comparable ionic conductivity to organic−inorganic SSE thin films are better suited for large-scale in-line processes. Additional processing steps inherent in organic−inorganic SSE thin-film composites, such as the incorporation of the organic separator or electrolyte material as an additional layer or as a dispersion in the inorganic matrix, as well as the curing of the organic layer, increase the manufacturing complexity and processing times. Even though the ionic conductivity of SSE pellets is comparable to that of the R-LLTO film, pellet manufacturing is not scalable due to longer

processing times, nontunability of thicknesses for large-scale production lines, and inferior mechanical properties.

3.5. Outlook and Future Work. Integrating this high-performance R-LLTO film into a complete battery would require investigations into cathode−electrolyte stability and anode−electrolyte stability to eliminate any detrimental phase changes at the interfaces that would jeopardize safety, reliability, and performance. Additionally, EIS studies to measure through-plane ionic conductivity would aid in better understanding Li⁺ transport through the film thickness, which is required to ensure that ion transport is not affected through the film depth. A double cantilever beam (DCB) fracture test of LLTO films to measure fracture energy/toughness would help to validate the fracture toughness estimated from the Vicker's hardness test and nanoindentation measurements. The use of printable techniques and rapid sintering is viable to produce an in-line process for solid-state battery production in open air with ultrahigh throughput.

4. CONCLUSIONS

In this work, we demonstrated a high-throughput approach that can be commercially relevant to produce robust and lightweight solid-state electrolytes in open air. The future of solid-state batteries hinges on the ability to develop low-cost and manufacturable SSEs. The significantly improved mechanical properties with among the highest fracture toughness and deformability with a low stiffness achieved by the R-LLTO SSE with micrometer-scale thicknesses are a key step for showcasing the prospect of solid-state battery technology. The key criterion for their success is ensuring that these have sufficient chemical and mechanical integrity to ensure that full contact remains between the active materials and the SSE without undesired side reactions during cycling. Given the mechanical compliance and softness of the R-LLTO SSE, this work could enable new paradigms for solid-state battery fabrication such as the detachment and direct lamination of R-LLTO SSEs to lithiated cathode films deposited on current collectors. Our work is a platform for the development of in-line, fully open-air solid-state batteries.

5. MATERIALS AND METHODS

5.1. Materials. The LLTO precursors for this work are Li_2CO_3 (99.0%, Sigma-Aldrich), La_2O_3 (99.0%, Sigma-Aldrich), and TiO_2 (99.0%, Sigma-Aldrich), which were stoichiometrically mixed and dispersed in isopropanol (IPA) according to the composition $Li_{0.3}La_{0.56}TiO_3$ with 10 wt % Li_2CO_3 added to account for potential Li loss during sintering. For wet ball milling, the precursors in IPA had a concentration 2 g of powder in 7 mL of IPA). Following ball milling, the LLTO precursor powder mixture in IPA was dried at 150 °C for 20 min on a hot plate in ambient and then dispersed in ethanol at a concentration of 600 mg/mL. Polyvinylpyrrolidone (Sigma-Aldrich, molecular weight of 360,000) with a concentration of 5 wt % (30 mg/mL) was added to the powder as a binder before deposition. Ted Pella, Inc. PELCO conductive silver paint, 30 g, was used as the silver ink for depositing electrodes on the R-LLTO film for in-plane EIS measurements.

5.2. Processing Equipment. Ball milling was done with a Retsch ball miller (MM200, agate grinding jar with 7 mm agate grinding balls). The LLTO precursor ink was deposited using spin coating (Laurell) or blade coating (Zehntner ZAA-2300). Sintering was performed using a rapid thermal processing

system shown in Figure S10 (AlWin21 RTP). The AlWin21 RTP system requires gas flow for the sintering process; a mixture of 80% O_2 and 20% N_2 gas was used to replicate atmospheric conditions. All experiments were conducted in an uncontrolled laboratory environment with 40% relative humidity.

5.3. Characterization Equipment.
Secondary electron (SE) and backscattered electron (BSE) imaging and semiquantitative energy-dispersive spectrometry (EDS) were performed using an electron microprobe analyzer (JEOL JXA-8530F). A high-resolution X-ray diffractometer (PANalytical X'Pert PRO MRD) was used for the grazing-angle diffraction experiment. Powder diffraction analysis was performed using a powder diffractometer (Malvern PANalytical Aeris research edition). Potentiostatic electrochemical impedance spectroscopy (EIS) measurements were performed in an in-plane configuration using ion blocking silver electrodes with a surface area of ~ 0.1 cm^2 and a parallel spacing of ~ 0.3 cm deposited on the LLTO thin film. The complex impedance response of the in-plane configuration was measured using a Paios measurement system (Fluxim AG) by varying the frequency from 10 Hz to 10 MHz for an applied voltage with an amplitude of 50 mV. Data from EIS measurements were fitted with simulated response of equivalent circuits using Fluxim's Characterization Suite software. The Vickers microhardness (H_v) was measured using a microhardness tester (hardness testing machine, Mitutoyo Corporation, Japan). A Keyence VHX-7000 microscope was used for optical characterization. A stylus profilometer (Tencor P-16) was used to measure SSE thickness and roughness. An X-ray photoelectron spectrometer (Kratos Axis Supra+) was used for surface material chemistry characterization. Nanoindentation was performed with the help of Nanoindenter XP along with the accompanying Nanosuite software. Two sets of a 5×5 array of indents made by a nanoindenter on the LLTO film were used to calculate the nanohardness and modulus of the LLTO thin film. The indents were performed using the continuous stiffness measurement (CSM) method. A Berkovich tip was utilized, and the depth limit for indents was set to be 2000 nm for the first set and 5000 nm for the second set along with a 1000 nm surface approach distance. The harmonic displacement target for the dynamic load portion of the method was set to be 2 nm with a frequency of 45 Hz.

5.4. Preparation of the LLTO Precursor Suspension and Synthesis of LLTO Thin Films.
5.4.1. Ball Milling. Wet ball milling was used to mix precursor powders Li_2CO_3, La_2O_3, and TiO_2 dispersed in IPA. Wet ball milling was chosen over dry ball milling because it was expected to reduce the size of the powder mixture (<10 μm) with less contamination and surface oxidation while maintaining a uniform particle size, despite the likelihood of having a slower rate of size reduction.[90,91] The ball milling machine used for wet ball milling is shown in Figure S10.

5.4.2. Drying and Binder Addition. The wet ball milled mixture was air dried by evaporating the IPA on a hot plate set to 120 °C. After drying, the powder mixture was dispersed in ethanol, and a 5 wt % polyvinylpyrrolidone (PVP) binder was added to this suspension. This suspension used for spin or blade coating is shown in Figure S10 (more details about the spin and blade coating process are discussed in the Results section). A wet ball milling mixture dispersed in IPA was not used directly as the suspension for spin or blade coating because the particle morphology in the as-wet ball milled IPA suspension may be flaky and less agglomerated rather than semispherical and agglomerated, which is more suitable for spin and blade coating

processes.[90,92] Ethanol was favored over IPA because it has a lower boiling point than IPA, which increases the rate of solvent evaporation during the baking step after the spin or blade coating process.[93] PVP was used as the binder because it is nontoxic and soluble in ethanol and has previously demonstrated to improve mechanical stability of SSEs.[94]

5.4.3. Open-Air Spin Coating and Blade Coating. The process flow for LLTO thin films from the precursor powder to the final SSE is shown in Figure S10. Films were initially deposited using spin coating. The precursor ink was statically dispensed on a silicon substrate and rotated at different speeds for various spin times. Following the rotating step, the spin-coated silicon substrate was baked for 5 to 10 min on a hot plate set to 100 °C to evaporate the residual solvent and allow thin-film formation. The effect of spin speed and time on particle distribution homogeneity in thin films was investigated using an optical microscope (Figure S11). Figure S11a–d shows optical images of the thin-film surfaces spin-coated at an ideal spin speed of 2000 rpm for different spin times (in s) of 10, 30, 60, and 180 s. As illustrated in Figure S11e, the optical images of thin-film surfaces were processed to contrast low film density areas (dark regions) with higher film density areas (brighter regions).

The maximum film coverage, characterized by a minimal overall dark area, was achieved for a spin coating time of 30 s, with a 10% cumulative dark region area, while thin films spin-coated for 15 and 180 s had a dark region area of nearly 20%. All these values are significantly too high because any detectable amount of dark areas represents gaps that would allow for Li dendrites to penetrate through the SSE and create a short circuit. Spin coating therefore was determined to not be the optimal method for producing LLTO films, and it also is not a scalable process method. Therefore, the blade coating process was used to process LLTO SSEs for the remainder of the study.

5.4.4. Rapid Thermal Annealing (RTA) to Form the LLTO Phase. The general RTA cycle used in this study is shown in Figure S12. Based on the literature, a hold temperature of 1100 °C was chosen for the sintering step in the RTA cycle to obtain the LLTO phase in spin-coated and blade-coated thin films.[57,95–97] Figure S13b–d shows images of samples spun at 2000 rpm with different sintering hold times of 10, 30, 60, and 180 s. The inset in Figure S13d shows a visually discolored LLTO film. This sample also had a nonuniform microstructure with elongated crystallites, as shown in Figure S3d. Therefore, we determined that sintering times longer than a minute can cause damage to the film and reduce the quality of the SSE film.

In fact, an LLTO phase was not obtained even for the optimized spin coating parameters and sintering time. Figure S14 compares spin-coated film XRD patterns after sintering for 30, 60, and 300 s compared with the $Li_{0.3}La_{0.56}TiO_3$ reference pattern and precursor phase LLTO. This comparison clearly demonstrates that all samples spin-coated and sintered for varying times have little or no structural match with the reference LLTO XRD spectrum and are much more like the precursor phase LLTO XRD spectrum. Based on the poor film density and morphology and the lack of the LLTO phase from spin coating, a more scalable open-air blade coating process was used to see if the LLTO phase could be produced.

Figures S15 and S16 show that blade coating produced a more uniform thin film at both the macro and micro levels. Upon varying the processing parameters, a processing speed of 300 cm/min and a blade height of 225 μm produced a uniform, dense, and approximately 10 μm-thick film. The XRD spectrum

of the film obtained after the blade coating and RTA step with a 1-min sintering hold time is shown in Figure 1. The obtained spectrum peaks largely correspond to the reference LLTO peak, indicating that the LLTO phase has indeed formed. Note that although the LLTO crystalline phase is the primary phase component in the film obtained after the blade coating and RTA steps, some amorphous LLTO precursor residue remains, as shown in Figure 1, and not all the LLTO precursor is converted into the LLTO crystalline phase. The implications of this will be discussed further below.

5.5. Thickness and Roughness of Blade-Coated LLTO Thin Films.

The thickness of the blade-coated sample was determined by scanning a profilometer probe across a 1000 μm one-dimensional (1D) line on the surface of the blade-coated sample. Figure S8 shows 1D surface profiles of five LLTO samples coated with blade heights of 245, 255, 265, 285, and 310 μm. A blade height of 245 μm produced a thin-film thickness of 10 μm and a smooth surface with an average roughness value of ± 0.6 μm. Figure S8 also shows a general trend of reduced roughness and thickness as the blade height decreases. The average film thickness increases by 60% for every 3% increase in average blade height. Thus, by adjusting the blade height, the film thickness can be tuned.

ASSOCIATED CONTENT

Supporting Information

The Supporting Information is available free of charge at https://pubs.acs.org/doi/10.1021/acsomega.3c03114.

(Figure S1) EDS spectra of spots shown in the BSE image of the LLTO film in Figure 2a,b; (Figure S2) EDS spectra of spots shown in the BSE image of the LLTO film in Figure 3a,b; (Figure S3) XPS analysis spots, N1, N2, M1, and M2 with optical images taken when the blade-coated LLTO samples were placed in the XPS instrument for analysis; (Figure S4) Li elemental spectrum of XPS analysis spots, N1, N2, M1, and M2; (Figure S5) C 1s elemental spectrum of the XPS analysis spot, N1, showing the peak indicating an O−C≡O bond; (Figure S6) schematic of the 2-electrode in-plane configuration used for EIS measurements and measured areas of Ag electrodes and the length between them; (Figure S7) load displacement curves for max displacement of 2000 nm vs 5000 nm; (Figure S8) surface roughness (R) for LLTO SSE thin films plotted as a function of blade height (H); (Figure S9) graph of SSE processing time vs ionic conductivity per thickness for the organic−inorganic thin film, inorganic thin film, and pellet SSEs compared to the blade-coated LLTO SSE thin film in this work; (Figure S10) process steps for fabricating LLTO thin-film SSEs with solution processing in open air; (Figure S11) VHX 7000 970F Analyzer software-processed optical images of the surfaces of thin films spin-coated at an ideal spin speed of 2000 rpm for different spin times and brightness spectrum of the optical image shown in Figure S1b with dark and bright regions corresponding to lower and higher thin-film density; (Figure S12) four-stage RTA cycle used for both spin coating and blade processes; (Figure S13) optical images of the microstructure and visual appearance of spin-coated films for LLTO films processed with different sintering hold times; (Figure S14) comparison of the spin-coated film XRD pattern with reference pattern $Li_{0.3}La_{0.56}TiO_3$ and amorphous LLTO after sintering; (Figure S15) optical and scanning electron microscope images of optimized LLTO blade-coated SSEs; (Figure S16) surface morphology of R-LLTO obtained using confocal microscopy imaging showing a dense film; (Table S1) La:Ti:O at. %, wt %, and corresponding molar composition obtained for EDS spots shown in Figure 5c,d; (Table S2) Average molar ratio of La, Ti, and O based on their visual appearance in the BSE image shown in Figure 2; (Table S3) Li:La:Ti:O wt % and corresponding molar composition obtained for spots, N1, N2, M1, and M2 using CasaXPS software; (Table S4) Comparison of the processing time and ion conduction values of R-LLTO with pellets, thin-film inorganic−organic composites, and inorganic thin films studied in the literature; (Table S5) elastic modulus and hardness of R-LLTO compared to other inorganic pellet and thin-film solid-state electrolytes studied in the literature (PDF)

AUTHOR INFORMATION

Corresponding Author

Nicholas Rolston — *Renewable Energy Materials and Devices Lab, School of Electrical, Computer and Energy Engineering (ECEE), Arizona State University, Tempe, Arizona 85287-5706, United States;* orcid.org/0000-0001-8093-1689; Email: nicholas.rolston@asu.edu

Authors

Mohammed Sahal — *Renewable Energy Materials and Devices Lab, School of Electrical, Computer and Energy Engineering (ECEE), Arizona State University, Tempe, Arizona 85287-5706, United States;* orcid.org/0000-0001-7664-074X

Jie Molloy — *Department of Applied Engineering Technology, North Carolina A&T State University, Greensboro, North Carolina 27411-0002, United States*

Venkateshwaran Ravi Narayanan — *School for Engineering of Matter, Transport & Energy, Ira A. Fulton Schools of Engineering, Arizona State University, Tempe, Arizona 85284, United States*

Leila Ladani — *School for Engineering of Matter, Transport & Energy, Ira A. Fulton Schools of Engineering, Arizona State University, Tempe, Arizona 85284, United States*

Xiaochuan Lu — *Department of Applied Engineering Technology, North Carolina A&T State University, Greensboro, North Carolina 27411-0002, United States;* orcid.org/0000-0003-0867-8644

Complete contact information is available at:
https://pubs.acs.org/10.1021/acsomega.3c03114

Notes

The authors declare no competing financial interest.

■ REFERENCES

(1) Diouf, B.; Pode, R. Potential of Lithium-Ion Batteries in Renewable Energy. *Renewable Energy* **2015**, *76*, 375−380.

(2) Killer, M.; Farrokhseresht, M.; Paterakis, N. G. Implementation of Large-Scale Li-Ion Battery Energy Storage Systems within the EMEA Region. *Appl Energy* **2020**, *260*, No. 114166.

(3) Stan, A.-I.; Świerczyński, M.; Stroe, D.-I.; Teodorescu, R.; Andreasen, S. J. Lithium Ion Battery Chemistries from Renewable Energy Storage to Automotive and Back-up Power Applications—An Overview. In *2014 International Conference on Optimization of Electrical and Electronic Equipment (OPTIM)*; IEEE, 2014; pp 713−720.

(4) Fergus, J. W. Ceramic and Polymeric Solid Electrolytes for Lithium-Ion Batteries. *J. Power Sources* **2010**, *195*, 4554−4569.

(5) Jung, K.; Shin, H.; Park, M.; Lee, J. Solid-state Lithium Batteries: Bipolar Design, Fabrication, and Electrochemistry. *ChemElectroChem* **2019**, *6*, 3842−3859.

(6) Takada, K. Progress and Prospective of Solid-State Lithium Batteries. *Acta Mater.* **2013**, *61*, 759−770.

(7) Wu, X.; Pan, K.; Jia, M.; Ren, Y.; He, H.; Zhang, L.; Zhang, S. Electrolyte for Lithium Protection: From Liquid to Solid. *Green Energy & Environment* **2019**, *4*, 360−374.

(8) Paul, P. P.; Chen, B.-R.; Langevin, S. A.; Dufek, E. J.; Weker, J. N.; Ko, J. S. Interfaces in All Solid State Li-Metal Batteries: A Review on Instabilities, Stabilization Strategies, and Scalability. *Energy Storage Mater* **2022**.

(9) Tan, D. H. S.; Meng, Y. S.; Jang, J. Scaling up High-Energy-Density Sulfidic Solid-State Batteries: A Lab-to-Pilot Perspective. *Joule* **2022**, 1755.

(10) Chen, S.; Wen, K.; Fan, J.; Bando, Y.; Golberg, D. Progress and Future Prospects of High-Voltage and High-Safety Electrolytes in Advanced Lithium Batteries: From Liquid to Solid Electrolytes. *J. Mater. Chem. A* **2018**, *6*, 11631−11663.

(11) Wang, Q.; Wang, H.; Wu, J.; Zhou, M.; Liu, W.; Zhou, H. Advanced Electrolyte Design for Stable Lithium Metal Anode: From Liquid to Solid. *Nano Energy* **2021**, *80*, No. 105516.

(12) Yang, C.; Fu, K.; Zhang, Y.; Hitz, E.; Hu, L. Protected Lithium-metal Anodes in Batteries: From Liquid to Solid. *Adv. Mater.* **2017**, *29*, 1701169.

(13) Yang, T.; Li, Y.; Chan, C. K. Enhanced Lithium Ion Conductivity in Lithium Lanthanum Titanate Solid Electrolyte Nanowires Prepared by Electrospinning. *J. Power Sources* **2015**, *287*, 164−169.

(14) Deiner, L. J.; Bezerra, C. A. G.; Howell, T. G.; Powell, A. S. Digital Printing of Solid-State Lithium-Ion Batteries. *Adv. Eng. Mater.* **2019**, *21*, 1900737.

(15) Zhu, Y.; Gonzalez-Rosillo, J. C.; Balaish, M.; Hood, Z. D.; Kim, K. J.; Rupp, J. L. M. Lithium-Film Ceramics for Solid-State Lithionic Devices. *Nat. Rev. Mater.* **2021**, *6*, 313−331.

(16) Liu, Q.; Geng, Z.; Han, C.; Fu, Y.; Li, S.; He, Y.; Kang, F.; Li, B. Challenges and Perspectives of Garnet Solid Electrolytes for All Solid-State Lithium Batteries. *J. Power Sources* **2018**, *389*, 120−134.

(17) Fergus, J. W. Recent Developments in Cathode Materials for Lithium Ion Batteries. *J. Power Sources* **2010**, *195*, 939−954.

(18) Minami, T.; Hayashi, A.; Tatsumisago, M. Recent Progress of Glass and Glass-Ceramics as Solid Electrolytes for Lithium Secondary Batteries. *Solid State Ionics* **2006**, *177*, 2715−2720.

(19) Monroe, C.; Newman, J. The Impact of Elastic Deformation on Deposition Kinetics at Lithium/Polymer Interfaces. *J. Electrochem. Soc.* **2005**, *152*, A396.

(20) Wolfenstine, J.; Allen, J. L.; Sakamoto, J.; Siegel, D. J.; Choe, H. Mechanical Behavior of Li-Ion-Conducting Crystalline Oxide-Based Solid Electrolytes: A Brief Review. *Ionics* **2018**, *24*, 1271−1276.

(21) Cao, D.; Sun, X.; Li, Q.; Natan, A.; Xiang, P.; Zhu, H. Lithium Dendrite in All-Solid-State Batteries: Growth Mechanisms, Suppression Strategies, and Characterizations. *Matter* **2020**, *3*, 57−94.

(22) Tang, Z.; Li, S.; Li, Y.; Xu, H.; Yu, Y.; Huang, Y.; Li, J. Lithium Metal Electrode Protected by Stiff and Tough Self-Compacting Separator. *Nano Energy* **2020**, *69*, No. 104399.

(23) Robertson, W. M.; Montgomery, D. J. Elastic Modulus of Isotopically-Concentrated Lithium. *Phys. Rev.* **1960**, *117*, 440.

(24) Bridgman, P. W. *The Effect of Tension on the Electrical Resistance of Certain Abnormal Metals*. In *Papers 32−58*; Harvard University Press, 1964; pp 1445−1470.

(25) Wolfenstine, J.; Go, W.; Kim, Y.; Sakamoto, J. Mechanical Properties of NaSICON: A Brief Review. *Ionics* **2023**, *29*, 1−8.

(26) Ke, X.; Wang, Y.; Ren, G.; Yuan, C. Towards Rational Mechanical Design of Inorganic Solid Electrolytes for All-Solid-State Lithium Ion Batteries. *Energy Storage Mater* **2020**, *26*, 313−324.

(27) Kravchyk, K. V.; Karabay, D. T.; Kovalenko, M. V. On the Feasibility of All-Solid-State Batteries with LLZO as a Single Electrolyte. *Sci. Rep.* **2022**, *12*, 1177.

(28) Kravchyk, K. V.; Kovalenko, M. V. Perspective on Design and Technical Challenges of Li-Garnet Solid-State Batteries. *Sci. Technol. Adv. Mater.* **2022**, *23*, 41−48.

(29) Liu, J.; Yuan, H.; Liu, H.; Zhao, C.; Lu, Y.; Cheng, X.; Huang, J.; Zhang, Q. Unlocking the Failure Mechanism of Solid State Lithium Metal Batteries. *Adv. Energy Mater.* **2022**, *12*, 2100748.

(30) Zhang, Y.; Zhao, Y.; Gosselink, D.; Chen, P. Synthesis of Poly (Ethylene-Oxide)/Nanoclay Solid Polymer Electrolyte for All Solid-State Lithium/Sulfur Battery. *Ionics* **2015**, *21*, 381−385.

(31) Bachman, J. C.; Muy, S.; Grimaud, A.; Chang, H.-H.; Pour, N.; Lux, S. F.; Paschos, O.; Maglia, F.; Lupart, S.; Lamp, P.; Giordano, L.; Shao-Horn, Y. Inorganic Solid-State Electrolytes for Lithium Batteries: Mechanisms and Properties Governing Ion Conduction. *Chem. Rev.* **2016**, *116*, 140−162.

(32) Balaish, M.; Gonzalez-Rosillo, J. C.; Kim, K. J.; Zhu, Y.; Hood, Z. D.; Rupp, J. L. M. Processing Thin but Robust Electrolytes for Solid-State Batteries. *Nat. Energy* **2021**, *6*, 227−239.

(33) Mei, A.; Wang, X.-L.; Lan, J.-L.; Feng, Y.-C.; Geng, H.-X.; Lin, Y.-H.; Nan, C.-W. Role of Amorphous Boundary Layer in Enhancing Ionic Conductivity of Lithium−Lanthanum−Titanate Electrolyte. *Electrochim. Acta* **2010**, *55*, 2958−2963.

(34) Bohnke, O.; Emery, J.; Fourquet, J.-L. Anomalies in Li+ Ion Dynamics Observed by Impedance Spectroscopy and 7Li NMR in the Perovskite Fast Ion Conductor (Li3xLa2/3-X□ 1/3-2x) TiO3. *Solid State Ionics* **2003**, *158*, 119−132.

(35) Aaltonen, T.; Alnes, M.; Nilsen, O.; Costelle, L.; Fjellvåg, H. Lanthanum Titanate and Lithium Lanthanum Titanate Thin Films Grown by Atomic Layer Deposition. *J. Mater. Chem.* **2010**, *20*, 2877−2881.

(36) Stramare, S.; Thangadurai, V.; Weppner, W. Lithium Lanthanum Titanates: A Review. *Chem. Mater.* **2003**, *15*, 3974−3990.

(37) Kitaoka, K.; Kozuka, H.; Hashimoto, T.; Yoko, T. Preparation of La0. 5Li0. 5TiO3 Perovskite Thin Films by the Sol−Gel Method. *J. Mater. Sci.* **1997**, *32*, 2063−2070.

(38) Inaguma, Y.; Liquan, C.; Itoh, M.; Nakamura, T.; Uchida, T.; Ikuta, H.; Wakihara, M. High Ionic Conductivity in Lithium Lanthanum Titanate. *Solid State Commun.* **1993**, *86*, 689−693.

(39) García-Martín, S.; Amador, U.; Morata-Orrantia, A.; Rodríguez-Carvajal, J.; Alario-Franco, M. Á. *Structure, Microstructur, Composition and Properties of Lanthanum Lithium Titanates and Some Substituted Analogues*. Wiley Online Library e2009.

(40) Hood, Z. D.; Zhu, Y.; Miara, L. J.; Chang, W. S.; Simons, P.; Rupp, J. L. M. A Sinter-Free Future for Solid-State Battery Designs. *Energy Environ. Sci.* **2022**, *15*, 2927−2936.

(41) Lobe, S.; Dellen, C.; Windmüller, A.; Tsai, C.-L.; Vondahlen, F.; Uhlenbruck, S.; Guillon, O. Challenges Regarding Thin Film Deposition of Garnet Electrolytes for All-Solid-State Lithium Batteries with High Energy Density. *Ionics (Kiel)* **2018**, *24*, 2199−2208.

(42) Gates-Rector, S.; Blanton, T. The Powder Diffraction File: A Quality Materials Characterization Database. *Powder Diffr.* **2019**, *34*, 352−360.

(43) Yang, T.; Gordon, Z. D.; Li, Y.; Chan, C. K. Nanostructured Garnet-Type Solid Electrolytes for Lithium Batteries: Electrospinning

Synthesis of Li7La3Zr2O12 Nanowires and Particle Size-Dependent Phase Transformation. *J. Phys. Chem. C* **2015**, *119*, 14947−14953.

(44) Weller, J. M.; Chan, C. K. Synthesis of Nanostructured Garnet. *Solid Electrolytes for Advanced Applications: Garnets and Competitors* 2019, 25−68, DOI: 10.1007/978-3-030-31581-8_2.

(45) Chan, C. K.; Yang, T.; Weller, J. M. Nanostructured Garnet-Type Li7La3Zr2O12: Synthesis, Properties, and Opportunities as Electrolytes for Li-Ion Batteries. *Electrochim. Acta* **2017**, *253*, 268−280.

(46) Guo, J.; Weller, J. M.; Yang, S.; Bhat, M. H.; Chan, C. K. Reactive Sintering of Garnet-Type Li6. 4La3Zr1. 4Ta0. 6O12 (LLZTO) from Pyrochlore Precursors Prepared Using a Non-Aqueous Sol−Gel Method. *Ionics* **2023**, 1−590.

(47) Sun, Y.-Q.; Luo, X.-T.; Zhu, Y.-S.; Liao, X.-J.; Li, C.-J. Li3PO4 Electrolyte of High Conductivity for All-Solid-State Lithium Battery Prepared by Plasma Spray. *J. Eur. Ceram. Soc.* **2022**, *42*, 4239−4247.

(48) Ping, W.; Wang, C.; Wang, R.; Dong, Q.; Lin, Z.; Brozena, A. H.; Dai, J.; Luo, J.; Hu, L. Printable, High-Performance Solid-State Electrolyte Films. *Sci. Adv.* **2020**, *6*, No. eabc8641.

(49) Ohnishi, T.; Takada, K. Sputter-Deposited Amorphous Li3PO4 Solid Electrolyte Films. *ACS Omega* **2022**, *7*, 21199−21206.

(50) Guo, Q.; Xu, F.; Shen, L.; Deng, S.; Wang, Z.; Li, M.; Yao, X. 20 Mm-Thick Li6. 4La3Zr1. 4Ta0. 6O12-Based Flexible Solid Electrolytes for All-Solid-State Lithium Batteries. *Energy Material Advances* 2022, DOI: 10.34133/2022/9753506.

(51) Koresh, I.; Klein, B. A.; Tang, Z.; Michaelis, V. K.; Troczynski, T. Li Ion Transport Properties of Amorphous/Crystalline Li-La-Zr-Nb-O Solid Electrolyte Thick Films Prepared by Suspension Plasma Spraying. *Solid State Ionics* **2022**, *380*, No. 115938.

(52) Xiong, L.; Ren, Z.; Xu, Y.; Mao, S.; Lei, P.; Sun, M. LiF Assisted Synthesis of LiTi2 (PO4) 3 Solid Electrolyte with Enhanced Ionic Conductivity. *Solid State Ionics* **2017**, *309*, 22−26.

(53) Symington, A. R.; Molinari, M.; Dawson, J. A.; Statham, J. M.; Purton, J.; Canepa, P.; Parker, S. C. Elucidating the Nature of Grain Boundary Resistance in Lithium Lanthanum Titanate. *J. Mater. Chem. A* **2021**, *9*, 6487−6498.

(54) Wu, J.-F.; Guo, X. Origin of the Low Grain Boundary Conductivity in Lithium Ion Conducting Perovskites: Li 3x La 0.67− x TiO 3. *Phys. Chem. Chem. Phys.* **2017**, *19*, 5880−5887.

(55) Luo, J. Interfacial Engineering of Solid Electrolytes. *Journal of Materiomics* **2015**, *1*, 22−32.

(56) Bowman, W. J.; Kelly, M. N.; Rohrer, G. S.; Hernandez, C. A.; Crozier, P. A. Enhanced Ionic Conductivity in Electroceramics by Nanoscale Enrichment of Grain Boundaries with High Solute Concentration. *Nanoscale* **2017**, *9*, 17293−17302.

(57) Ban, C. W.; Choi, G. M. The Effect of Sintering on the Grain Boundary Conductivity of Lithium Lanthanum Titanates. *Solid State Ionics* **2001**, *140*, 285−292.

(58) Geng, H.; Mei, A.; Lin, Y.; Nan, C. Effect of Sintering Atmosphere on Ionic Conduction and Structure of Li0. 5La0. 5TiO3 Solid Electrolytes. *Mater. Sci. Eng., B* **2009**, *164*, 91−95.

(59) Zhang, S.; Zhao, H.; Guo, J.; Du, Z.; Wang, J.; Świerczek, K. Characterization of Sr-Doped Lithium Lanthanum Titanate with Improved Transport Properties. *Solid State Ionics* **2019**, *336*, 39−46.

(60) Zhao, W.; Yi, J.; He, P.; Zhou, H. Solid-State Electrolytes for Lithium-Ion Batteries: Fundamentals Challenges and Perspectives. *Electrochemical Energy Reviews* **2019**, *2*, 574−605.

(61) Ladani, L.; Harvey, E.; Choudhury, S. F.; Taylor, C. R. Effect of Varying Test Parameters on Elastic−Plastic Properties Extracted by Nanoindentation Tests. *Exp Mech* **2013**, *53*, 1299−1309.

(62) Anstis, G. R.; Chantikul, P.; Lawn, B. R.; Marshall, D. B. A Critical Evaluation of Indentation Techniques for Measuring Fracture Toughness: I, Direct Crack Measurements. *J. Am. Ceram. Soc.* **1981**, *64*, 533−538.

(63) Cho, Y.-H.; Wolfenstine, J.; Rangasamy, E.; Kim, H.; Choe, H.; Sakamoto, J. Mechanical Properties of the Solid Li-Ion Conducting Electrolyte: Li 0.33 La 0.57 TiO 3. *J. Mater. Sci.* **2012**, *47*, 5970−5977.

(64) Hu, X.; Qiang, W.; Huang, B. Preparation and Properties of LixLa0. 5TiO3 Perovskite Oxide Electrolytes. *J. Am. Ceram. Soc.* **2017**, *100*, 4153−4158.

(65) Han, G.; Kinzer, B.; Garcia-Mendez, R.; Choe, H.; Wolfenstine, J.; Sakamoto, J. Correlating the Effect of Dopant Type (Al, Ga, Ta) on the Mechanical and Electrical Properties of Hot-Pressed Li-Garnet Electrolyte. *J. Eur. Ceram. Soc.* **2020**, *40*, 1999−2006.

(66) Yu, S.; Schmidt, R. D.; Garcia-Mendez, R.; Herbert, E.; Dudney, N. J.; Wolfenstine, J. B.; Sakamoto, J.; Siegel, D. J. Elastic Properties of the Solid Electrolyte Li7La3Zr2O12 (LLZO). *Chem. Mater.* **2016**, *28*, 197−206.

(67) Luo, Y.; Feng, W.; Meng, Z.; Wang, Y.; Jiang, X.; Xue, Z. Interface Modification in Solid-State Lithium Batteries Based on Garnet-Type Electrolytes with High Ionic Conductivity. *Electrochim. Acta* **2021**, *397*, No. 139285.

(68) Hu, S.; Xu, P.; de Vasconcelos, L. S.; Stanciu, L.; Ni, H.; Zhao, K. Elastic Modulus, Hardness, and Fracture Toughness of Li6. 4La3Zr1. 4Ta0. 6O12 Solid Electrolyte. *Chin. Phys. Lett.* **2021**, *38*, No. 098401.

(69) Wolfenstine, J.; Jo, H.; Cho, Y.-H.; David, I. N.; Askeland, P.; Case, E. D.; Kim, H.; Choe, H.; Sakamoto, J. A Preliminary Investigation of Fracture Toughness of Li7La3Zr2O12 and Its Comparison to Other Solid Li-Ionconductors. *Mater. Lett.* **2013**, *96*, 117−120.

(70) Athanasiou, C. E.; Jin, M. Y.; Ramirez, C.; Padture, N. P.; Sheldon, B. W. High-Toughness Inorganic Solid Electrolytes via the Use of Reduced Graphene Oxide. *Matter* **2020**, *3*, 212−229.

(71) Yan, G. *Mechanical Behavior of Solid Electrolyte Materials for Lithium-Ion Batteries*. RWTH Aachen University 2020.

(72) Valle, J. M.; Huang, C.; Tatke, D.; Wolfenstine, J.; Go, W.; Kim, Y.; Sakamoto, J. Characterization of Hot-Pressed von Alpen Type NASICON Ceramic Electrolytes. *Solid State Ionics* **2021**, *369*, No. 115712.

(73) Smith, S.; Thompson, T.; Sakamoto, J.; Allen, J.; Baker, D. R.; Wolfenstine, J. Electrical, Mechanical and Chemical Behavior of Li1. 2Zr1. 9Sr0. 1 (PO4) 3. *Solid State Ionics* **2017**, *300*, 38−45.

(74) Kim, K. J.; Balaish, M.; Wadaguchi, M.; Kong, L.; Rupp, J. L. M. Solid-state Li−Metal Batteries: Challenges and Horizons of Oxide and Sulfide Solid Electrolytes and Their Interfaces. *Adv. Energy Mater.* **2021**, *11*, 2002689.

(75) Kalnaus, S.; Westover, A. S.; Kornbluth, M.; Herbert, E.; Dudney, N. J. Resistance to Fracture in the Glassy Solid Electrolyte Lipon. *J. Mater. Res.* **2021**, *36*, 787−796.

(76) Orisekeh, K. *Processing of Composite Carbon Materials and Solid Electrolytes for Supercapicitor Energy Storage*, 2022.

(77) Chen, X.; Du, Y.; Chung, Y.-W. Commentary on Using H/E and H3/E2 as Proxies for Fracture Toughness of Hard Coatings. *Thin Solid Films* **2019**, *688*, No. 137265.

(78) McPherson, R. A Review of Microstructure and Properties of Plasma Sprayed Ceramic Coatings. *Surf Coat Technol* **1989**, *39-40*, 173−181.

(79) Golozar, M.; Paolella, A.; Demers, H.; Savoie, S.; Girard, G.; Delaporte, N.; Gauvin, R.; Guerfi, A.; Lorrmann, H.; Zaghib, K. Direct Observation of Lithium Metal Dendrites with Ceramic Solid Electrolyte. *Sci. Rep.* **2020**, *10*, 1−11.

(80) Cooper, C.; Sutorik, A. C.; Wright, J.; Luoto, E. A., III; Gilde, G.; Wolfenstine, J. Mechanical Properties of Hot Isostatically Pressed Li0. 35La0. 55TiO3. *Adv. Eng. Mater.* **2014**, *16*, 755−759.

(81) Liu, G.; Li, T.; Xing, Y.; Pan, W. Synthesis of Li7La3Zr2O12Solid Electrolyte by Solid Phase Sintering Method. In *IOP Conference Series: Materials Science and Engineering*; IOP Publishing, 2019; Vol. *678*, p 012150.

(82) Lv, R.; Kou, W.; Guo, S.; Wu, W.; Zhang, Y.; Wang, Y.; Wang, J. Preparing Two-Dimensional Ordered Li0.33La0.557TiO3 Crystal in Interlayer Channel of Thin Laminar Inorganic Solid-State Electrolyte towards Ultrafast Li+ Transfer. *Angew. Chem., Int. Ed.* **2022**, *61*, No. e202114220.

(83) Xia, W.; Xu, B.; Duan, H.; Tang, X.; Guo, Y.; Kang, H.; Li, H.; Liu, H. Reaction Mechanisms of Lithium Garnet Pellets in Ambient Air: The Effect of Humidity and CO2. *J. Am. Ceram. Soc.* **2017**, *100*, 2832−2839.

(84) Ma, J.; Jiang, H.; Chen, L.; Wu, Y.; Liu, Y.; Ping, W.; Song, X.; Xiang, H. Interfacial Optimization between Cathode and 20 Mm-

Thickness Solid Electrolyte Membrane via in-Situ Polymerization for Lithium Metal Batteries. *J. Power Sources* **2022**, *537*, No. 231517.

(85) Yuan, B.; Zhao, B.; Wang, Q.; Bai, Y.; Cheng, Z.; Cong, Z.; Lu, Y.; Ji, F.; Shen, F.; Wang, P.-F.; Han, X. A Thin Composite Polymer Electrolyte with High Room-Temperature Conductivity Enables Mass Production for Solid-State Lithium-Metal Batteries. *Energy Storage Mater* **2022**, *47*, 288−296.

(86) Li, Y.; Yang, L.; Dong, R.; Zhang, T.; Yuan, J.; Liu, Y.; Liu, Y.; Sun, Y.; Zhong, B.; Chen, Y.; Wu, Z.; Guo, X. A High Strength Asymmetric Polymer−Inorganic Composite Solid Electrolyte for Solid-State Li-Ion Batteries. *Electrochim. Acta* **2022**, *404*, No. 139701.

(87) Liu, G.; Shi, J.; Zhu, M.; Weng, W.; Shen, L.; Yang, J.; Yao, X. Ultra-Thin Free-Standing Sulfide Solid Electrolyte Film for Cell-Level High Energy Density All-Solid-State Lithium Batteries. *Energy Storage Mater.* **2021**, *38*, 249−254.

(88) Yu, G.; Wang, Y.; Li, K.; Chen, D.; Qin, L.; Xu, H.; Chen, J.; Zhang, W.; Zhang, P.; Sun, Z. Solution-Processable Li 10 GeP 2 S 12 Solid Electrolyte for a Composite Electrode in All-Solid-State Lithium Batteries. *Sustainable Energy Fuels* **2021**, *5*, 1211−1221.

(89) Zhang, B.; Tan, R.; Yang, L.; Zheng, J.; Zhang, K.; Mo, S.; Lin, Z.; Pan, F. Mechanisms and Properties of Ion-Transport in Inorganic Solid Electrolytes. *Energy Storage Mater.* **2018**, *10*, 139−159.

(90) Jung, H. J.; Sohn, Y.; Sung, H. G.; Hyun, H. S.; Shin, W. G. Physicochemical Properties of Ball Milled Boron Particles: Dry vs Wet Ball Milling Process. *Powder Technol.* **2015**, *269*, 548−553.

(91) Miao, C.; Hamad, W. Y. Controlling Lignin Particle Size for Polymer Blend Applications. *J. Appl. Polym. Sci.* **2017**, *134* (), DOI: 10.1002/app.44669.

(92) Siddheswaran, R.; Mangalaraja, R.; Tijerina, E. P.; Menchaca, J.-L.; Melendrez, M. F.; Avila, R. E.; Jeyanthi, C. E.; Gomez, M. E. Fabrication and Characterization of a Diluted Magnetic Semi-conducting TM Co-Doped Al: ZnO (TM= Co, Ni) Thin Films by Sol−Gel Spin Coating Method. *Spectrochim. Acta, Part A* **2013**, *106*, 118−123.

(93) Wypych, G Alcohols. In *Databook of Solvents*; Wypych, G., Eds.; ChemTec Publishing, 2014; pp 53−116, DOI: 10.1016/B978-1-895198-66-9.50006-0

(94) Aslan, M.; Weingarth, D.; Jäckel, N.; Atchison, J. S.; Grobelsek, I.; Presser, V. Polyvinylpyrrolidone as Binder for Castable Supercapacitor Electrodes with High Electrochemical Performance in Organic Electrolytes. *J. Power Sources* **2014**, *266*, 374−383.

(95) Schröckert, F.; Schiffmann, N.; Bucharsky, E. C.; Schell, K. G.; Hoffmann, M. J. Tape Casted Thin Films of Solid Electrolyte Lithium-Lanthanum-Titanate. *Solid State Ionics* **2018**, *328*, 25−29.

(96) de Oliveira, R. B.; Andreeta, M. R. B.; de Souza, D. M. P. F.; Rodrigues, J. E. F. S.; Pizani, P. S. Innovative Design for the Enhancement of Lithium Lanthanum Titanate Electrolytes. *Cryst. Growth Des.* **2019**, *19*, 4897−4901.

(97) Chen, C. H.; Amine, K. Ionic Conductivity, Lithium Insertion and Extraction of Lanthanum Lithium Titanate. *Solid State Ionics* **2001**, *144*, 51−57.